# Abaqus implementation of phase-field model for brittle fracture

Mohammed A. Msekh [a,b,*], Juan Michael Sargado [b], Mostafa Jamshidian [c], Pedro Miguel Areias [d], Timon Rabczuk [b,e]

[a] Civil Engineering Department, College of Engineering, University of Babylon, Babylon, Iraq
[b] Institute of Structural Mechanics, Faculty of Civil Engineering, Bauhaus-University Weimar, Germany
[c] Department of Mechanical Engineering, Isfahan University of Technology, Isfahan, Iran
[d] Departamento de Física, Universidade de Évora, Portugal
[e] School of Civil, Environmental and Architectural Engineering, Korea University, Republic of Korea

## ABSTRACT

A phase-field model for brittle fracture is implemented in the commercial finite element software Abaqus by means of UEL and UMAT subroutines. The phase-field method considerably reduces the implementation complexity for fracture problems as it removes the need for numerical tracking of discontinuities in the displacement field that are characteristic of discrete crack methods. This is accomplished by replacing the sharp discontinuities with a scalar damage phase-field representing the diffuse crack topology wherein the amount of diffusion is controlled by a regularization parameter. The nonlinear coupled system consisting of the linear momentum equation and a diffusion-type equation governing the phase-field evolution is solved simultaneously via a Newton–Raphson approach. The implemented crack propagation model does not require predefined paths for crack growth or user-defined surfaces to simulate crack debonding. Post-processing of simulation results is performed via an additional subroutine implemented in the visualization module.

© 2014 Elsevier B.V. All rights reserved.

## 1. Introduction

The detection of failure mechanisms in structures due to crack initiation and growth via numerical modeling is of great importance in engineering applications, and has continually been the subject of attention by many researchers. For brittle materials, the underlying theory is generally based on the thermodynamic framework first introduced by Griffith [1] wherein the effect of crack formation is quantified via a surface energy term that is dependent on the material surface tension, referred to as the *critical energy release rate*. A number of methods are currently available that deal specifically with numerical simulation of fracture initiation and growth. Such methods may usually be classified under one of two broad categories: *discrete* versus *smeared/diffuse* approaches.

Discrete crack models originally stemmed from the work of Ngo and Scordelis [2] and function by modifying the existing finite element mesh according to the evolution of the crack topology. In early implementations, incorporation of the crack as a geometrical entity was accomplished via node splitting which constrained the crack path to lie along element edges. This results in mesh dependency of the solution especially for complex crack patterns. Improvements to the original method were subsequently introduced in order to alleviate the mesh bias problem, for instance in the work of Ingraffea and Saouma on automatic remeshing [3]. The discrete crack approach has also been successfully applied to problems involving crack propagation along material interfaces [4,5]. More recently, a 3D inter-element separation model was developed by Zhou and Molinari [6] in which a cohesive surface element is dynamically inserted between two tetrahedral elements whenever the critical stress state is reached. As with the original discrete crack model, the crack may only propagate along existing element edges. In lieu of remeshing, the issue of mesh dependency is addressed in [6] by varying the strength of the cohesive elements according to a Weibull model. A drawback of constraining crack propagation to occur only along element edges without applying additional correction is that the fracture energy is over-estimated when the true crack path deviates significantly from the corresponding element edge orientation, especially when the mesh is coarse. The extended finite element method [7,8] based on enrichment within a partition of unity framework is another important development coming from the group of Belytschko in the late 90s, and has been the focus of intense research. In the XFEM, the crack topology is represented implicitly, usually by means of level

* Corresponding author at: Institute of Structural Mechanics, Faculty of Civil Engineering, Bauhaus-University Weimar, Germany.
*E-mail addresses:* mohammed.msekh@uni-weimar.de (M.A. Msekh), timon.rabczuk@uni-weimar.de (T. Rabczuk).

sets. This enables cracks to propagate completely independent of the underlying mesh. Furthermore, known characteristics of the phenomena being modeled are incorporated into the numerical solution space by enrichment of the standard finite element shape functions with expressions derived from benchmark analytical solutions. This endows the method with huge flexibility, such as the ability to resolve stress singularities at the crack tip as well as model the true stress behavior at the tip vicinity using a much coarser discretization than would normally be necessary in the absence of any enrichment. The implicit crack representation technique has also been successfully combined with numerical methods based on strain-smoothing as demonstrated in the work of Chen et al. [9], and with meshfree approaches in particular the Element Free Galerkin (see for example Rabczuk et al. [10]). However, XFEM is not without its disadvantages. In 2D for example, a single crack segment requires a pair of level set functions for the definition of its topology, so that computational complexity increases with the number of individual crack segments, as does the problem size due to the incorporation of additional degrees of freedom. An alternative means of discrete crack representation based on partition of unity enrichment is via cohesive segments, implemented within the finite element context by Remmers et al. [11], and within a meshfree setting by Rabczuk and Belytschko [12]. In these methods, the crack topology is represented by a set of discrete, overlapping segments. The method may also be carried out without using shape function enrichment, as demonstrated in Rabczuk et al. [13].

On the other hand, the smeared crack model was pioneered by Rashid [14], who used it to perform simulations involving concrete applications. Rather than attempting to model the actual crack topology, smeared approaches incorporate the effects associated with crack formation such as stress release into the constitutive model. In an initially isotropic material, the emergence of a tensile crack alters the constitutive behavior from isotropic to orthotropic due to the loss of stiffness in the direction normal to crack, which is also referred to as the *plane of degradation*. Since no additional degrees of freedom are added, crack evolution can be simulated using standard finite element codes without modification of the initial mesh. The original model used by Rashid [14] is known as a *fixed crack model* due to the fact that for subsequent loadings the orientation of the POD at a given Gauss point is fixed at the orientation initially calculated when the strength criterion for cracking is met. Later on, Cope et al. [15] introduced the so-called *rotating crack model* wherein the orientation of the POD is adjusted to match the current major principal direction in order to account for the phenomenon of secondary cracking. It is well known that the traditional approach of utilizing a strength criterion to determine crack extension produces non-objective results owing to the presence of stress singularities at the crack tip, i.e. it is possible to advance the crack to an adjacent element with increasingly less load simply by refining the mesh [16]. This problem may be overcome by adopting energetic approaches, such as constitutive models based on the *fictitious crack model* of Hillerborg et al. [17] which utilize the fracture energy as a material parameter in addition to the tensile strength. However this leads to another type of mesh bias problem stemming from the energy release rate being influenced by the element size. In the *Crack Band Model* proposed by Bažant and Oh [18] this issue was addressed by adjusting the value of the softening modulus based on the element size or the Gauss point tributary areas so that the correct value of the critical energy release rate is preserved during crack extension. To this end, a characteristic length parameter is introduced into the model, termed the *crack band width*. Still, this does not allow for arbitrarily large elements since a critical element size then emerges for which the softening modulus is infinite, implying a straight drop of the stress–strain curve after reaching the peak stress. Further scaling beyond this point (for elements larger than the critical size) would result in the material exhibiting spurious snap-back behavior.

In recent years, phase-field methods for fracture simulations have been gaining popularity among researchers. Phase-field methods also fall under the broader class of smeared/diffuse crack approaches, however they differ from the earlier models in their reliance on a *variational* theory of fracture. This is itself a relatively recent concept, being developed in the late 90s by Francfort and Marigo [19] to overcome certain limitations associated with the classical Griffith theory such as its inability to predict crack initiation and branching, as well as handle curved crack paths. In the variational theory, the total energy potential is assumed to include a surface term associated with the energy required for the formation of a crack. That is,

$$\Psi = \Psi^b + \Psi^s = \int_{\Omega \backslash \Gamma} \psi(\boldsymbol{\varepsilon}) \, d\Omega + \int_{\Gamma} \mathcal{G}_c \, d\Gamma \qquad (1)$$

This potential is then simultaneously minimized with respect to the displacement field and the crack geometry, with the idea being that the fracture topology evolution should occur in such a way that results in minimal potential energy. Further developments were introduced by Bourdin et al. [20,21], the most notable being the regularization of the sharp crack topology into a diffuse entity defined via a scalar variable (later termed the *phase-field*) which serves to interpolate between cracked and intact states of the material. Bourdin et al. [20] utilized an evolution equation for the phase-field derived from the Mumford–Shah functional for image segmentation. Kuhn and Müller [22] alternatively proposed an evolution equation of the Ginzburg–Landau type and mentioned that the application of a phase field approach to crack propagation is possible after taking the irreversible character of crack propagation into account. Noting that the steady state problem associated with the phase-field evolution equation yields a solution of exponential type, Kuhn and Müller [23] developed new finite elements with exponential shape functions and demonstrated their superior performance compared to standard Lagrange elements in cases where the crack path aligns with element edges. A modification of the original functional proposed in [20] was made by Lancioni and Royer-Carfagni [24] to handle problems involving deviatoric-type fracture. However, while their model correctly does not allow for material inter-penetration it is also unable to model crack-opening, hence limiting its applicability to cases where the dominant stress behavior is compressive. Amor et al. [25] improved the prior model to be able to handle crack opening by allowing degradation of stiffness corresponding to the spherical component of the stress when the value of said component is positive (signifying volumetric expansion). Significant contributions to the theory were also made by Miehe et al. [26,27] in the form of a thermodynamically consistent framework for brittle mode-I fracture for the case of rate-independent as well as viscous material response. In particular, their formulation ensures local irreversibility of the phase-field which permits the correct simulation of material behavior for cyclic loading. Whereas in [26] the coupled system consisting of stress equilibrium equations and the phase-field evolution is solved simultaneously (with local growth of the phase field imposed via a penalty term), a staggered scheme is employed in [27] in which a local energy history field is introduced as a state variable to ensure irreversible crack growth.

In the present work, we implement the phase-field method for simulating brittle mode-I fracture within the Abaqus software by means of UEL subroutines. Abaqus/Standard allows for five different types of fracture criteria to be used for crack-growth simulations. These are: critical stress at a certain distance ahead of the crack tip, critical crack opening displacement, crack length versus time, VCCT (the Virtual Crack Closure Technique), and the

low-cycle fatigue criterion based on the Paris law to model quasi-static crack growth. However all of these models require a predefined crack path and the definition of two distinct but initially bonded contact surfaces along which the crack will propagate. This implies the inclusion of master and slave surfaces during construction of the geometric model, as well as the specification of node sets to identify the initially bonded part of slave surfaces. Clearly, a phase-field approach offers the advantage of avoiding the aforementioned complications related to geometry construction and meshing, in addition to offering the ability to model multiple crack initiation, branching and coalescence for complex structures in which no prior knowledge of the crack paths are available.

The content of the paper is as follows: in Section 2 we discuss the theory pertaining to the diffuse representation of crack surfaces by means of a phase-field, and the corresponding modification of the total potential energy functional to account for the said field. In Section 3, we derive the appropriate expressions for the tangent stiffness matrix and right hand side vector corresponding to a two dimensional element with three degrees of freedom per node (two for the displacement field and one for the phase-field). Section 4 contains the details for implementing the phase-field method in an Abaqus UEL subroutine. A separate UMAT subroutine is also implemented in order to be able to visualize results in the Abaqus viewer. Numerical examples are given in Section 5 consisting of different benchmark problems, followed by concluding remarks in Section 6.

## 2. Phase-field representation of crack surface

Let us consider the 1D problem consisting of an infinitely long cylindrical bar (constant cross-sectional area $A$) that is aligned along the $x$-axis and fully cut by a crack at $x = a$ as shown in Fig. 1. The surface energy dissipated by the formation of the said crack may be calculated simply as the product of the critical energy release rate $\mathcal{G}_c$ and the crack surface equal to the cross sectional area of the bar, i.e.

$$\Psi^s = \int_{\Gamma_s} \mathcal{G}_c \, d\Gamma = \mathcal{G}_c A \tag{2}$$

However such a calculation implies knowledge of the crack path, and while this is trivial in 1D, the actual crack topology is needed in higher dimensions to be able to compute the value of $A$. An alternative is to smooth out the crack such that the surface energy can be calculated as a domain integral. As demonstrated in Miehe et al. [26], this can be accomplished by introducing a scalar field variable to represent the diffuse crack of the form

$$\phi(x) = \exp\left(\frac{-|x - a|}{\ell_0}\right) \tag{3}$$

where $\phi(x)$ is denoted as the crack phase field, and $\ell_0$ is a parameter that controls the amount of "diffusion" of the crack. It can be seen that $\phi(x) \in [0, 1]$, with 0 representing a completely intact state of the material, and 1 a fully broken state. The crack phase field for the 1D problem described above is shown in Fig. 2 for different values of $\ell_0$. It should be emphasized that $\ell_0$ does not represent the actual "width" of the diffuse crack. On the contrary, the form of expression (3) means that the crack is smoothed out over the *entire* domain, since $\phi(x)$ is never actually zero. Furthermore, while (3)

may not be the only possible expression for describing the diffuse crack, the choice of functions is not entirely arbitrary. In particular, $\phi(x)$ should be symmetric, as well as monotonically decay to zero as we move away from the crack location. That is,

$$\phi(x) \to 0 \text{ as } x \to \pm\infty \tag{4a}$$

$$\phi'(x) \to 0 \text{ as } x \to \pm\infty \tag{4b}$$

Taking derivatives of (3), we obtain

$$\phi'(x) = -\frac{\text{sgn}(x - a)}{\ell_0} \exp\left(-\frac{|x - a|}{\ell_0}\right)$$

$$\phi''(x) = \left[\frac{\text{sgn}(x - a)}{\ell_0}\right]^2 \exp\left(-\frac{|x - a|}{\ell_0}\right) \tag{5}$$

$$= \frac{1}{\ell_0^2} \exp\left(-\frac{|x - a|}{\ell_0}\right) = \frac{1}{\ell_0^2} \phi(x)$$

These derivatives are undefined at $x = a$, however for $x \neq a$ the expression in (3) satisfies the ODE

$$-\phi''(x) + \frac{1}{\ell_0^2} \phi(x) = 0 \tag{6}$$

as reported in [26]. The weak formulation corresponding to the above equation along with the derivative boundary conditions given in (4b) is

$$0 = \int_{-\infty}^{\infty} v'\phi' + \frac{1}{\ell_0^2} v\phi \, dx \tag{7}$$

where $v$ represents some test function. The associated quadratic functional is then given by

$$I(\phi) = \int_{-\infty}^{\infty} \frac{1}{2}\left[(\phi')^2 + \frac{1}{\ell_0^2}\phi^2\right] dx \tag{8}$$

The construction of $I(\phi)$ implies that (6) along with (4b) constitute the Euler–Lagrange equations associated with the variational problem

$$\phi^\star = \arg\inf_{\phi \in W}\{I(\phi)\} \tag{9}$$

in which $W$ is the set of functions satisfying (4b) along with the internal condition $\phi(a) = 1$. Furthermore, $\phi^\star$ is none other than the function given in (3). Plugging this into the functional in (8) yields

$$I(\phi^\star) = \int_{-\infty}^{\infty} \frac{1}{\ell_0^2} \exp\left(-\frac{2|x - a|}{\ell_0}\right) dx = \frac{1}{\ell_0} \tag{10}$$
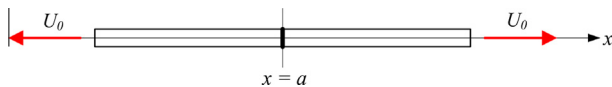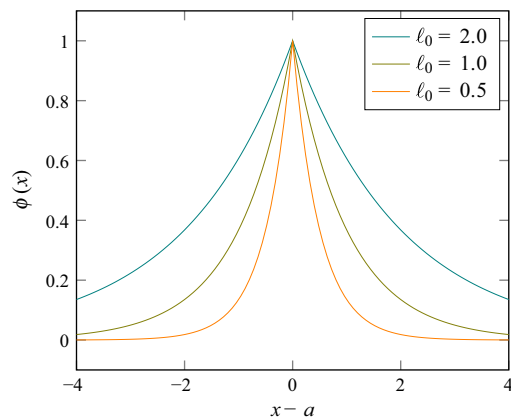
**Fig. 2.** Crack phase-field $\phi$ for different values of $\ell_0$.

**Fig. 1.** 1D bar cut by a crack.

Hence we can define a function

$$\gamma(\phi) = \frac{1}{2}\left[\ell_0(\phi')^2 + \frac{1}{\ell_0}\phi^2\right] \tag{11}$$

which is simply the integrand of (8) scaled by $\ell_0$ so that the regularized surface energy may now be written as a domain integral:

$$\Psi^s = \mathcal{G}_c\int_\Omega \gamma(\phi)\,d\Omega = \mathcal{G}_c\int_A\int_{-\infty}^{\infty}\gamma(\phi)\,dx\,dA = \mathcal{G}_c A \tag{12}$$

Correspondingly, the bulk energy is recast as

$$\Psi^b = \int_\Omega g(\phi)\psi^e(\varepsilon)\,d\Omega \tag{13}$$

in which $g(\phi)$ is known as the *stress degradation function*. A common form obtained from [26] and other works is

$$g(\phi) = (1-\phi)^2 + k \tag{14}$$

where $k$ is a parameter chosen to be as small as possible while at the same time keeping the system of equations well-conditioned. It is worthwhile to note that parameter $a$ representing the crack location does not appear in (12), which means that no preliminary estimation of the crack path is required. This endows the phase-field model with enormous flexibility, such as the automatic nucleation, branching and merging of cracks. The expression given in (11) may be readily extended to 2D and 3D, with the relevant form being

$$\gamma(\phi) = \frac{1}{2}\left[\ell_0\frac{\partial\phi}{\partial x_i}\frac{\partial\phi}{\partial x_i} + \frac{1}{\ell_0}\phi^2\right] \tag{15}$$

where $i = 1,\ldots,d$ with $d$ being the number of dimensions.

## 3. Governing equations and finite element model

By using the results from the previous section, the total potential energy functional can be written as

$$\Psi(\phi,\mathbf{u}) = \int_\Omega\left[(1-\phi)^2 + k\right]\psi(\varepsilon)\,d\Omega \\ + \int_\Omega\frac{\mathcal{G}_c}{2}\left[\ell_0\nabla\phi\cdot\nabla\phi + \frac{1}{\ell_0}\phi^2\right]d\Omega \tag{16}$$

where for a linear-elastic material, $\psi(\varepsilon) = \frac{1}{2}\lambda\varepsilon_{kk}\varepsilon_{ll} + \mu\varepsilon_{ij}\varepsilon_{ij}$ with $\lambda$ and $\mu$ being the Láme constants. We confine ourselves to the case of small strains, i.e. $\varepsilon_{ij} = \frac{1}{2}\left(\partial u_i/\partial x_j + \partial u_j/\partial x_i\right)$. The governing equations are obtained as follows: we first define the first variation of the external work increment (dropping terms that evaluate to zero) as

$$\delta W_{ext} = \int_\Omega b_j\delta u_j\,d\Omega + \int_{\partial\Omega}h_j\delta u_j\,d\partial\Omega \tag{17}$$

where $b_j$ and $h_j$ are the components of the body force and boundary traction respectively. On the other hand, the variation of the internal energy increment is given by

$$\delta W_{int} = \delta\Psi = \frac{\partial\Psi}{\partial\varepsilon_{ij}}\delta\varepsilon_{ij} + \frac{\partial\Psi}{\partial\phi}\delta\phi \tag{18}$$

which for the case of (16) yields

$$\delta\Psi = \int_\Omega\left[(1-\phi)^2 + k\right]\sigma_{ij}\delta\varepsilon_{ij}\,d\Omega + \int_\Omega -2(1-\phi)\delta\phi\psi(\varepsilon)\,d\Omega \\ + \int_\Omega\mathcal{G}_c\left(\ell_0\frac{\partial\phi}{\partial x_i}\frac{\partial\delta\phi}{\partial x_i} + \frac{1}{\ell_0}\phi\delta\phi\right)d\Omega \tag{19}$$

By appropriate transfer of differentiation between variables, it can be shown that the above expression is equivalent to

$$\delta\Psi = \int_{\partial\Omega}\left[(1-\phi)^2 + k\right]n_i\sigma_{ij}\delta u_j\,d\partial\Omega \\ - \int_\Omega\left[(1-\phi)^2 + k\right]\frac{\partial\sigma_{ij}}{\partial x_i}\delta u_j\,d\Omega \\ + \int_\Omega -2(1-\phi)\delta\phi\psi(\varepsilon)\,d\Omega + \int_{\partial\Omega}\frac{\partial\phi}{\partial x_i}n_i\delta\phi\,d\partial\Omega \\ + \int_\Omega\mathcal{G}_c\left(-\ell_0\frac{\partial^2\phi}{\partial x_i\partial x_i}\delta\phi + \frac{1}{\ell_0}\phi\delta\phi\right)d\Omega \tag{20}$$

where $n_i$ denote the components of the unit vector normal to the surface $d\Omega$. We then combine the terms in (17) and (20), imposing that $\delta W_{int} - \delta W_{ext} = 0$ should hold for arbitrary values of $\delta u_i$ and $\delta\phi$. This leads to the strong form of the governing equations:

$$\left[(1-\phi)^2 + k\right]\frac{\partial\sigma_{ij}}{\partial x_i} + b_j = 0 \text{ in } \Omega \tag{21a}$$

$$\left[(1-\phi)^2 + k\right]n_i\sigma_{ij} = h_j \text{ on } \partial\Omega_h \tag{21b}$$

$$u_j = \bar{u}_j \text{ on } \partial\Omega_u \tag{21c}$$

$$-\mathcal{G}_c\ell_0\frac{\partial^2\phi}{\partial x_i\partial x_i} + \left[\frac{\mathcal{G}_c}{\ell_0} + 2\psi(\varepsilon)\right]\phi = 2\psi(\varepsilon) \text{ in } \Omega \tag{21d}$$

$$\frac{\partial\phi}{\partial x_i}n_i = 0 \text{ on } \partial\Omega \tag{21e}$$

The above shows a coupled system consisting of the modified stress equilibrium Eq. (21a) and the phase-field evolution Eq. (21d). Eqs. (21b) and (21c) are the natural and essential boundary conditions associated with (21a), while the last equation is the natural boundary condition associated with (21d). Note that while satisfaction of (21e) seems trivial, it implies an upper limit to the choice of the regularization parameter $\ell_0$ with respect to the domain such that the phase-field sufficiently decays to zero at the boundary.

Since the finite element model is based on the weak form, it is more convenient to work with Eqs. (17) and (19) directly. Utilizing the Voigt notation in a 2D setting, the primary variables can be discretized as follows

$$\mathbf{u} = \sum_{I=1}^{m}\mathbf{N}_I^{\mathbf{u}}\mathbf{u}_I, \quad \phi = \sum_{I=1}^{m}N_I\phi_I \tag{22}$$

in which

$$\mathbf{N}_I^{\mathbf{u}} = \begin{bmatrix} N_I & 0 \\ 0 & N_I \end{bmatrix} \tag{23}$$

where $N_I$ denotes the shape function associated with node $I$, and $\mathbf{u}_I = \{u_x, u_y\}_I^{\mathsf{T}}$ and $\phi_I$ are the displacement and phase-field values at node $I$. In this work have chosen to employ the standard 4-node quadrilateral element so that $m = 4$. The corresponding derivative quantities are given by

$$\varepsilon = \sum_{I=1}^{m}\mathbf{B}_I^{\mathbf{u}}\mathbf{u}_I, \quad \nabla\phi = \sum_{I=1}^{m}\mathbf{B}_I^{\phi}\phi_I \tag{24}$$

with

$$\mathbf{B}_I^{\mathbf{u}} = \begin{bmatrix} N_{I,x} & 0 \\ 0 & N_{I,y} \\ N_{I,y} & N_{I,x} \end{bmatrix} \quad \mathbf{B}_I^{\phi} = \begin{bmatrix} N_{I,x} \\ N_{I,y} \end{bmatrix} \tag{25}$$

Correspondingly, the test functions and there derivatives are discretized as

$$\delta\mathbf{u} = \sum_{I=1}^{m}\mathbf{N}_I^{\mathbf{u}}\delta\mathbf{u}_I, \quad \delta\phi = \sum_{I=1}^{m}N_I\delta\phi_I$$
$$\delta\varepsilon = \sum_{I=1}^{m}\mathbf{B}_I^{\mathbf{u}}\delta\mathbf{u}_I, \quad \nabla\delta\phi = \sum_{I=1}^{m}\mathbf{B}_I^{\phi}\delta\phi_I \tag{26}$$

Using the above expressions and invoking the arbitrariness of the test functions, we obtain the external force from (17) as

$$\mathbf{f}_{Iext}^{\mathbf{u}} = \int_{\Omega} \mathbf{N}_I^{\mathbf{u}T} \mathbf{b} + \int_{\partial\Omega} \mathbf{N}_I^{\mathbf{u}T} \mathbf{h} \qquad (27)$$

Likewise, the internal forces are obtained from (19) as

$$\mathbf{f}_{Iint}^{\mathbf{u}} = \int_{\Omega} \left[ (1-\phi)^2 + k \right] \mathbf{B}_I^{\mathbf{u}T} \boldsymbol{\sigma} \, d\Omega \qquad (28)$$

so that the discrete equations corresponding to stress equilibrium may be expressed as via the following residual:

$$\mathbf{r}_I^{\mathbf{u}} = \mathbf{f}_{Iint}^{\mathbf{u}} - \mathbf{f}_{Iext}^{\mathbf{u}} = \int_{\Omega} \left[ (1-\phi)^2 + k \right] \mathbf{B}_I^{\mathbf{u}T} \boldsymbol{\sigma} \, d\Omega - \int_{\Omega} \mathbf{N}_I^{\mathbf{u}T} \mathbf{b} - \int_{\partial\Omega} \mathbf{N}_I^{\mathbf{u}T} \mathbf{h} \qquad (29)$$

On the other hand, the residual corresponding to the evolution of the phase-field is given by

$$r_I^{\phi} = \sum_{J=1}^m \int_{\Omega} \mathcal{G}_c \ell_0 \mathbf{B}_I^{\phi T} \nabla\phi + \left[ \frac{\mathcal{G}_c}{\ell_0} + 2\psi(\boldsymbol{\varepsilon}) \right] N_I \phi \, d\Omega$$
$$- \int_{\Omega} 2N_I \psi(\boldsymbol{\varepsilon}) \, d\Omega \qquad (30)$$

We seek the solution for which the $\mathbf{r}^{\mathbf{u}} = \mathbf{0}$ and $\mathbf{r}^{\phi} = 0$. Due to the nonlinear nature of the residuals with respect to $\mathbf{u}$ and $\phi$, we employ an incremental-iterative strategy utilizing the Newton–Raphson approach in conjunction with a parametrization based on a fictitious time $t$:

$$\left\{ \begin{matrix} \mathbf{u} \\ \phi \end{matrix} \right\}_{t+\Delta t} = \left\{ \begin{matrix} \mathbf{u} \\ \phi \end{matrix} \right\}_t - \begin{bmatrix} \mathbf{K}^{\mathbf{uu}} & \mathbf{K}^{\mathbf{u}\phi} \\ \mathbf{K}^{\phi\mathbf{u}} & \mathbf{K}^{\phi\phi} \end{bmatrix}_t^{-1} \left\{ \begin{matrix} \mathbf{r}^{\mathbf{u}} \\ \mathbf{r}^{\phi} \end{matrix} \right\}_t \qquad (31)$$
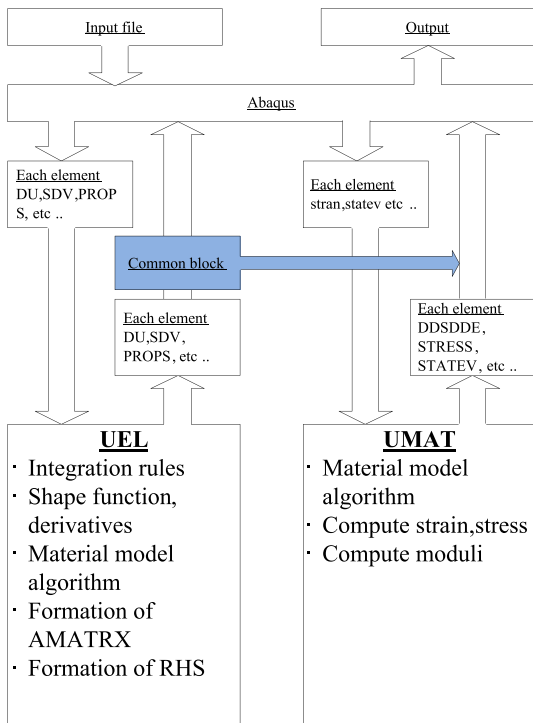


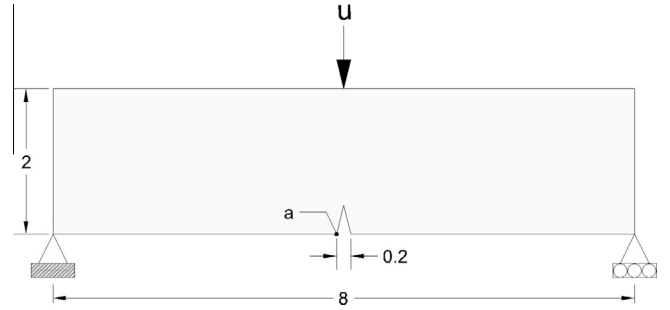**Fig. 3.** Abaqus implementation of phase-field method using UEL and UMAT subroutines.



**Fig. 4.** Three points bending simply supported beam. Geometry, loading and boundary conditions.
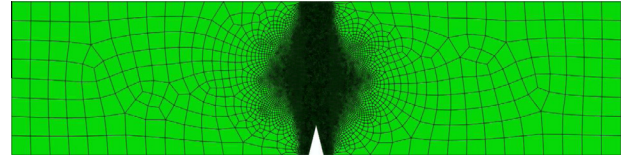


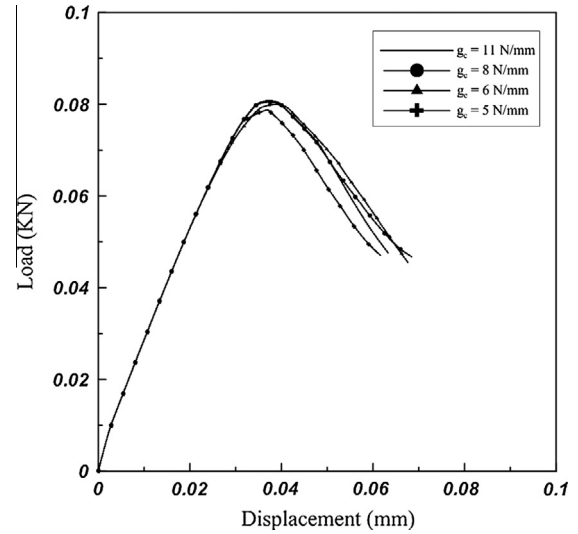**Fig. 5.** Mesh refinement of the three points bending sample.



**Fig. 6.** Load–displacement curve for different values of $\mathcal{G}_c$.

in which

$$\mathbf{K}_{IJ}^{\mathbf{uu}} = \frac{\partial \mathbf{r}_I^{\mathbf{u}}}{\partial \mathbf{u}_J} = \int_{\Omega} \left[ (1-\phi)^2 + k \right] \mathbf{B}_I^{\mathbf{u}T} \mathbf{C} \mathbf{B}_J^{\mathbf{u}} \, d\Omega \qquad (32a)$$

$$\mathbf{K}_{IJ}^{\mathbf{u}\phi} = \frac{\partial \mathbf{r}_I^{\mathbf{u}}}{\partial \phi_J} = \int_{\Omega} -2(1-\phi) \mathbf{B}_I^{\mathbf{u}T} \boldsymbol{\sigma} N_J \, d\Omega \qquad (32b)$$

$$\mathbf{K}_{IJ}^{\phi\mathbf{u}} = \frac{\partial \mathbf{r}_I^{\phi}}{\partial \mathbf{u}_J} = \int_{\Omega} -2(1-\phi) N_I \boldsymbol{\sigma}^T \mathbf{B}_J^{\mathbf{u}} \, d\Omega \qquad (32c)$$

$$\mathbf{K}_{IJ}^{\phi\phi} = \frac{\partial \mathbf{r}_I^{\phi}}{\partial \phi_J} = \int_{\Omega} \mathcal{G}_c \ell_0 \mathbf{B}_I^{\phi T} \mathbf{B}_J^{\phi} + \left[ \frac{\mathcal{G}_c}{\ell_0} + 2\psi(\boldsymbol{\varepsilon}) \right] N_I N_J \, d\Omega \qquad (32d)$$

It should be noted that the above system does not guarantee irreversible evolution of the phase-field, i.e. that $\phi_{t+\Delta t} \geqslant \phi_t$. This can be approximately enforced by introducing a penalty term to the phase-field equation as described in Miehe et al. [26]. Let us define the following function
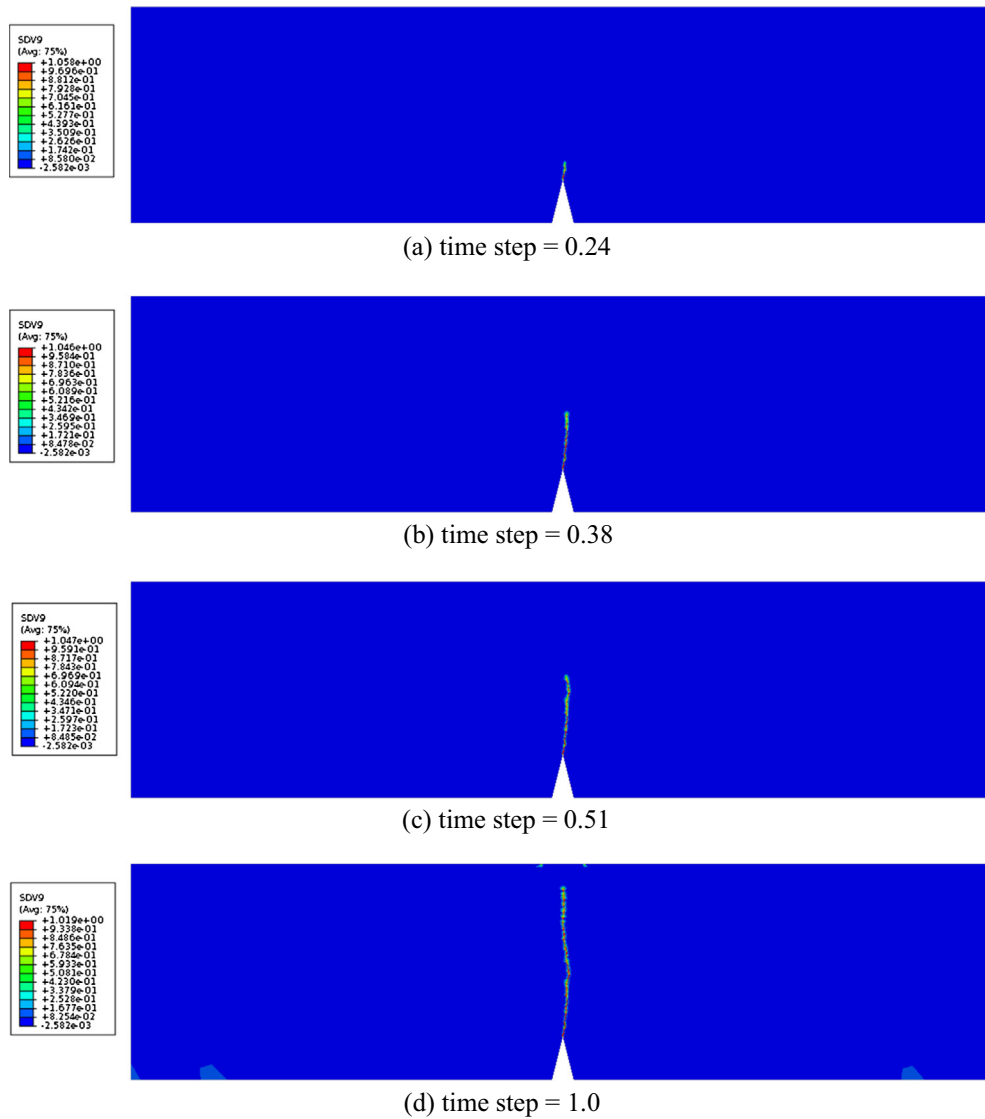
(a) time step = 0.24



(b) time step = 0.38



(c) time step = 0.51



(d) time step = 1.0

**Fig. 7.** Three points bending test. Crack propagation for a mesh with 17,363 elements, element size $h = 0.01$ mm with length-scale parameter $l = 0.03$ mm.
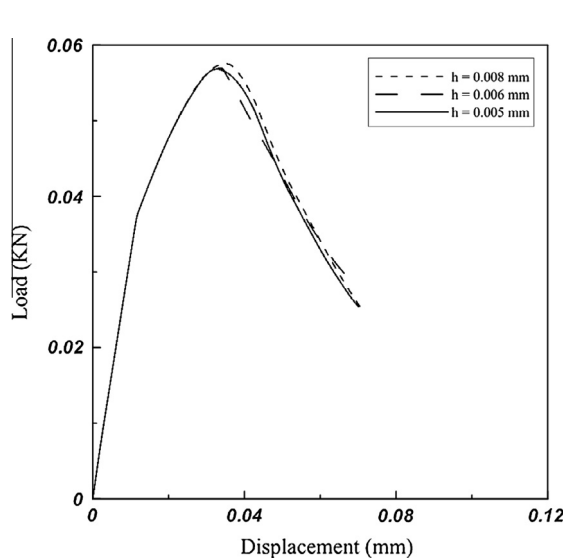


**Fig. 8.** Effect of mesh size one the load–displacement curve for the three-point bending test.
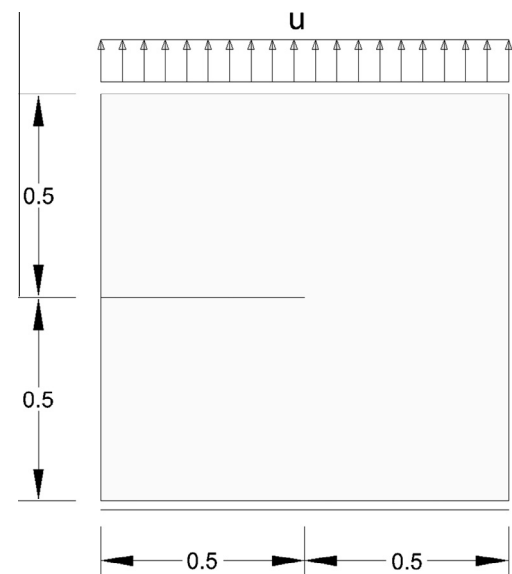


**Fig. 9.** Geometry, loading and boundary conditions for the notched plate.
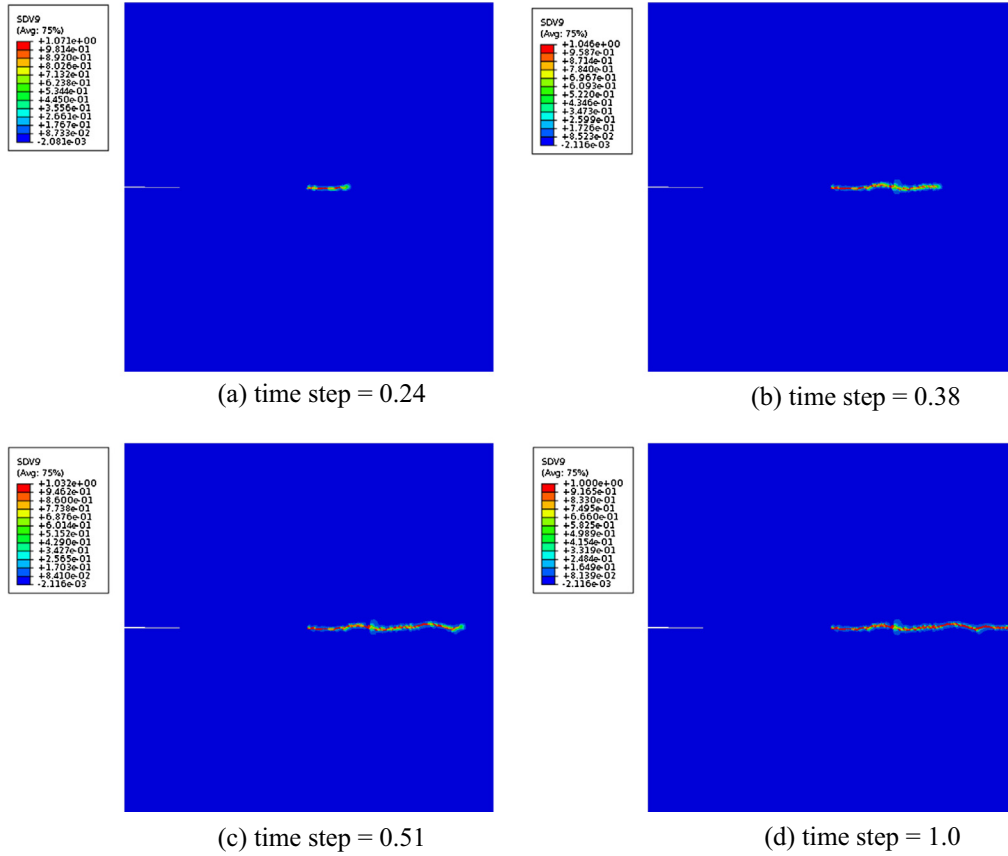
(a) time step = 0.24



(b) time step = 0.38



(c) time step = 0.51



(d) time step = 1.0

**Fig. 10.** Notched plate tension test. Crack propagation (a)–(d) for a mesh with 12,672 elements, $h = 0.005$ and $\ell_0 = 0.015$ mm.
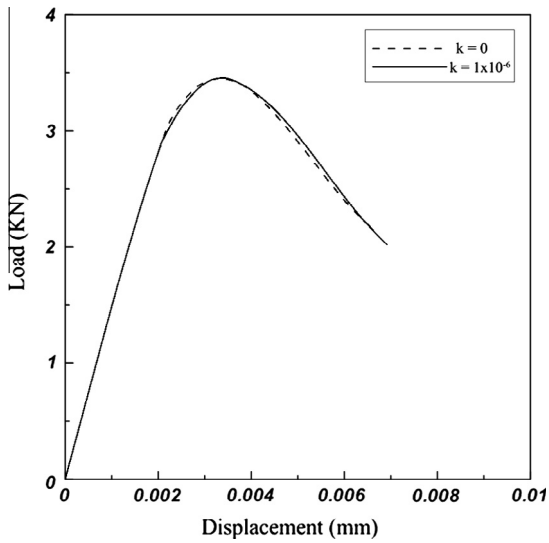


**Fig. 11.** Load–displacement curve for notched plate in tension.



**Fig. 12.** Load–displacement curve for notched plate in tension for different values of $\mathcal{G}_c$.

$$\langle x \rangle_{-} = \begin{cases} -x, & x < 0 \\ 0, & x \geqslant 0 \end{cases} \tag{33}$$

A suitable penalty term can be constructed as

$$P(\dot{\phi}) = \frac{\eta}{n\Delta t} \langle \dot{\phi} \rangle_{-}^{n} \tag{34}$$

where $n$ is a positive integer which in the present work is taken to be equal to 2, and $\dot{\phi} = \phi_{t+\Delta t} - \phi_t$. The parameter $\eta$ controls the
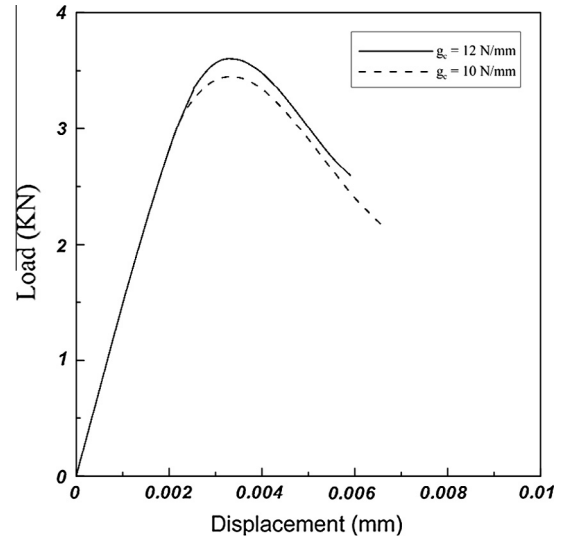
magnitude of the penalty term, and should be set to a value that is large enough to sufficiently enforce the irreversibility condition, but not too large as to result in an ill-conditioned system. The residual and the system Jacobian are then modified as follows:

$$r_I^{\phi} = \sum_{J=1}^{m} \int_{\Omega} \mathcal{G}_c \ell_0 \mathbf{B}_I^{\phi T} \nabla \phi + \left[ \frac{\mathcal{G}_c}{\ell_0} + 2\psi(\boldsymbol{\varepsilon}) \right] N_I \phi \, d\Omega$$
$$- \int_{\Omega} 2N_I \left[ \psi(\boldsymbol{\varepsilon}) - \frac{\eta}{n\Delta t} \dot{\phi}^n \right] d\Omega \tag{35}$$
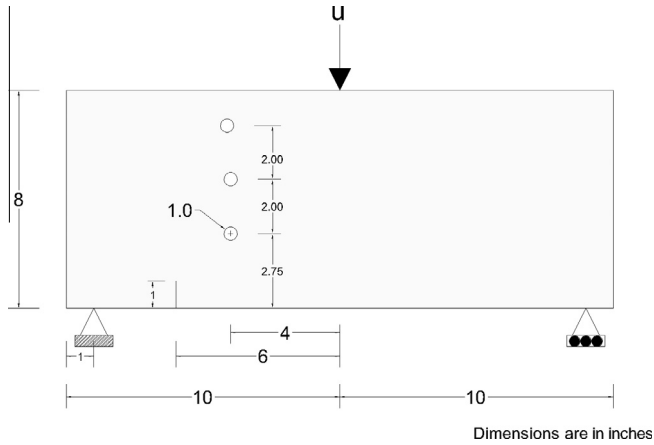
**Fig. 13.** Geometry, loading and boundary conditions for simply supported notched beam with three openings.
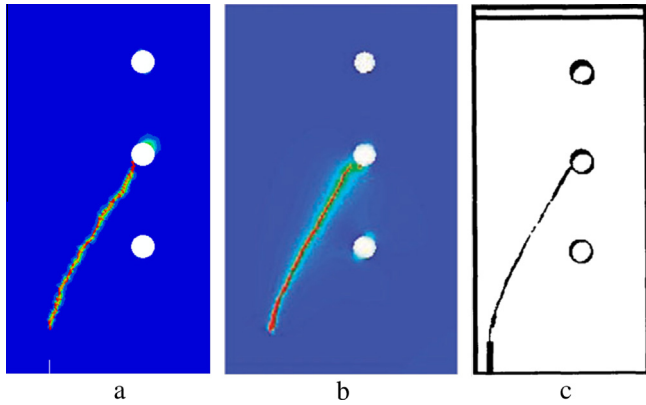


**Fig. 14.** Comparison the crack patterns for the benchmark of notched three-points bending test: (a) crack patterns with 25,285 elements, $h$ = 0.05 mm and $l$ = 0.2 mm, (b) crack patterns by Miehe et al. [26], (c) Digitized photo of crack pattern from by Bittencourt et al. [31]

$$\mathbf{K}_{IJ}^{\phi\phi} = \int_{\Omega} \mathcal{G}_c \ell_0 \mathbf{B}_I^{\phi T} \mathbf{B}_J^{\phi} + \left[\frac{\mathcal{G}_c}{\ell_0} + 2\psi(\boldsymbol{\varepsilon})\right] N_I N_J \, d\Omega + \int_{\Omega} \frac{\eta}{\Delta t} \dot{\phi}_-^{n-1} N_I N_J \, d\Omega$$

(36)

## 4. Abaqus implementation

The system of equations resulting from the above finite element model is nonlinear so that one must resort to incremental-iterative schemes for calculating the solution. We have chosen to implement the above-mentioned model within the software Abaqus in order to take advantage of its built-in nonlinear solver employing the Newton–Raphson algorithm as well as automatic time-stepping schemes.

With regard to the phase-field model for brittle fracture in 2D, we define a 4-node quadrilateral element with 3 degrees of freedom per node, which are respectively $u_x$, $u_y$ and $\phi$. This is implemented using the UEL subroutine in Abaqus which allows for user-defined calculation of element tangent stiffness matrices as well as nodal force vectors (right hand side). The constitutive behavior at the element Gauss points is evaluated via a call to a material function that is defined within the UEL subroutine. Hence, the user-programmed UEL subroutine is called for each element, which in turn makes several calls to the material function

according to the number of Gauss points per element. The UEL subroutine interfaces with standard arrays defined in the Abaqus environment for the retrieval of values of dependent variables such as the displacement and phase-field, and also for storing internal/ state variables associated with each Gauss point.

One drawback of using UEL subroutines is that post-processing and visualization of the results is not straightforward. In particular, it is not possible to trivially display the results in the Abaqus Viewer, i.e. since element shape functions are user-defined, the software can no longer automatically extrapolate variables from Gauss points to the element nodes. One way to address this problem is by coding a python script that accesses the database to obtain (and if necessary, recalculate) results in such a way that is compatible with some existing element type in the Abaqus library. Alternatively, element results can be stored as state-dependent variables [28], which is valid if the connectivity and shape functions of the user-defined element are the same as for an existing Abaqus implementation. Otherwise there will be errors arising from the differences between the element formulations. We have applied the latter approach in this work, as the shape functions for our user defined elements are simply the standard Q4 shape functions. Visualization is implemented by utilizing a second, *fictitious* mesh consisting of native Abaqus elements that matches the original mesh of user-defined elements.

The material for the overlaid mesh is defined via a UMAT user subroutine, which is also used for computing stresses and tangent moduli at the integration points. The material parameters are chosen such that there is no resistance to strain, i.e. we use an elastic material with Young's modulus set near to machine precision $(10^{-15})$. The state variables for the integration points are stored in the array STATEV which is accessible by the UMAT subroutine. These variables are originally calculated within the UEL subroutine and stored in the built-in array SVARS that is accessible by that subroutine. Transfer of values from SVARS to the STATEV array is accomplished by making use of the `common` statement, albeit with the effect of somewhat slower execution speed. Fig. 3 shows the relation between the different subroutines.

## 5. Numerical examples

### 5.1. Three-point bending test

The aim of this benchmark is to test the model in a bending problem and verify the crack propagation and compare it with the recent literature [26]. Fig. 4 shows the geometric setup of the benchmark with the loading conditions. The benchmark descretized into (17,363) quadrilateral elements with an effective mesh size $h = 0.01$ mm in the refined region near the initial notch. The material parameters are used as $E = 20.8$ GPa and $v = 0.3$. The critical energy release rate is $\mathcal{G}_c = 5$ N/mm. The load applied in a one step with a minimum load increment ($\Delta u = 1 \times 10^{-7}$ mm) and maximum load increment ($\Delta u = 1 \times 10^{-2}$ mm) using the automatic time incrementation of Abaqus. The mesh discretization is shown in Fig. 5 with element edge lengths equal to 0.01 mm at the expected crack path and 0.25 mm at areas well removed from the crack trajectory. Fig. 6 shows the load deflection curve of a reference point (a) in Fig. 4 and it is compared with different values of the energy release rate $\mathcal{G}_c$. Fig. 6 shows the effect of increasing the value of $\mathcal{G}_c$ on the value of the collapse load. The progression of the crack at several load levels is shown in Fig. 7. In Fig. 8 different simulations are carried out to show the comparison of the load–displacement curve for different values of element edge sizes at the crack path vicinity. The edge sizes used varied from 0.008 mm, 0.006 mm and 0.005 mm with the corresponding number of elements being 24,400, 31,944 and 34,711 respectively. The material

parameters are $E = 20.8$ GPa and $v = 0.3$ and the energy release rate is $\mathcal{G}_c = 5$ N/mm with length scale parameter $\ell_0 = 0.015$ mm.

## 5.2. Notched square plate subject to tension

The problem of a square plate with an initial notch subjected to tensile loading has been analyzed in Miehe et al. [26,27] and Borden [29] using Isogeometric Analysis. The geometric setup as well as loading conditions are shown in Fig. 9. In the present work, the notch is modeled as an actual feature of the geometry. Alternatively, it is possible to avoid having to include the notch in the geometry by solving the steady state problem

$$-\ell_0 \nabla^2 \phi + \frac{1}{\ell_0} \phi = 0 \qquad (37)$$

over the entire square plate, subject to homogeneous natural boundary conditions plus an internal condition of $\phi = 1$ at the notch. The geometry is meshed using 12,672 elements with manual refinement resulting in an effective element size of $h = 0.005$ within the expected crack propagation zone. Young's modulus and Poisson's ratio were chosen to be equal to 210 GPa and 0.3 respectively, while the critical energy release rate $\mathcal{G}_c$ was set to a value of 10 N/mm. The applied loading consists of an imposed displacement at the top portion of the plate, with the bottom of the plate fixed. The loading is applied incrementally and linearly with respected to time by using the command AMPLITUDE = RAMP in the Abaqus input file. The initial time increment was chosen to be $\Delta u_0 = 10^{-2}$ mm, with succeeding increments being allowed to vary according to the automatic time stepping scheme available in Abaqus, but with a minimum
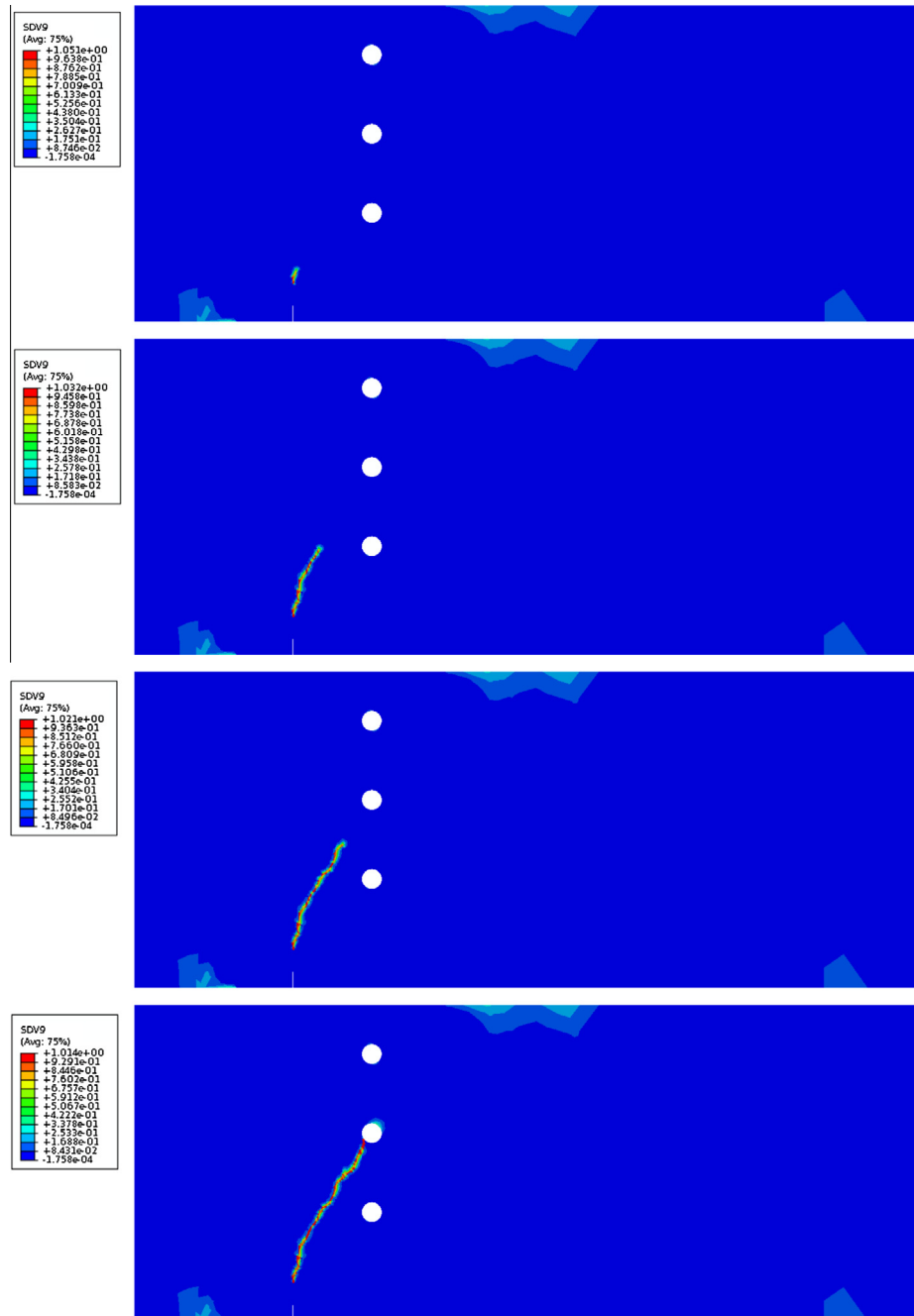


**Fig. 15.** Three-point bending test. Crack propagation (a)–(d) for a mesh with 25,285 elements, element size $h = 0.05$ mm with length-scale parameter $\ell_0 = 0.15$ mm.
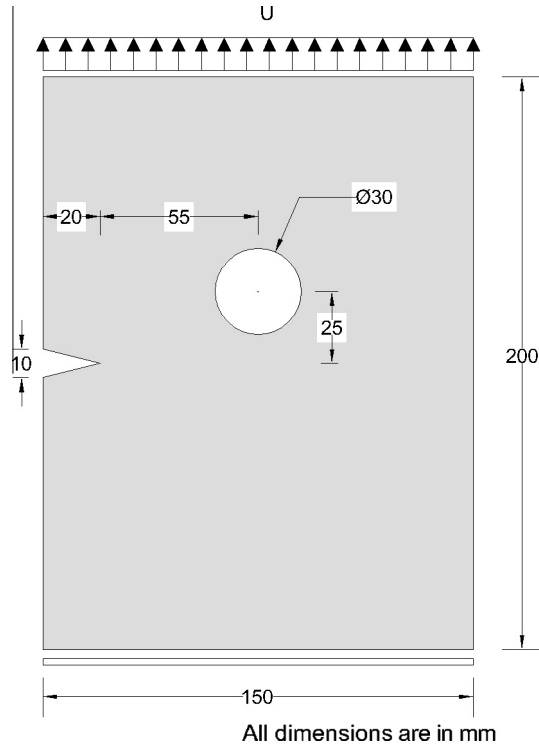
**Fig. 16.** Notched rectangular specimen with opening. Geometry, loading and boundary conditions.

allowed time increment of $10^{-7}$ mm. A value of 0.015 mm was selected for the crack regularization parameter $\ell_0$, following the recommendation in Miehe et al. [26] that $\ell_0$ should be more than twice the characteristic element length in order to properly resolve the crack. The crack propagation at different time steps is shown in Fig. 10, and the resulting load–displacement curve is given in Fig. 11, wherein it is also shown that setting the parameter $k$ equal to zero does not make system ill-conditioned. Fig. 12 shows the effect on the load–displacement curve of increasing the value of the critical energy release rate $\mathcal{G}_c$.

### 5.3. Notched beam with three openings

The Ingraffea–Bittencourt benchmark is one of the most popular examples for validating curved crack patterns. The experimental testing was carried out by Ingraffea and Grigoriu [30], with subsequent numerical modeling by Bittencourt et al. [31]. The geometry and the loading of the problem are given in Fig. 13. In the present study, we have used the following values for material parameters: Young's modulus $E = 20$ GPa, Poisson ratio $v = 0.3$, and critical energy release rate $\mathcal{G}_c = 1$ N/mm. Fig. 14 compares the results of present study with the experimental crack pattern as well as numerical results from Miehe et al. [26] and shows that the present Abaqus implementation is able to predict the correct trajectory of a curved crack. Fig. 15 shows four different time steps of crack propagation with 25,285 elements which are used in simulations.
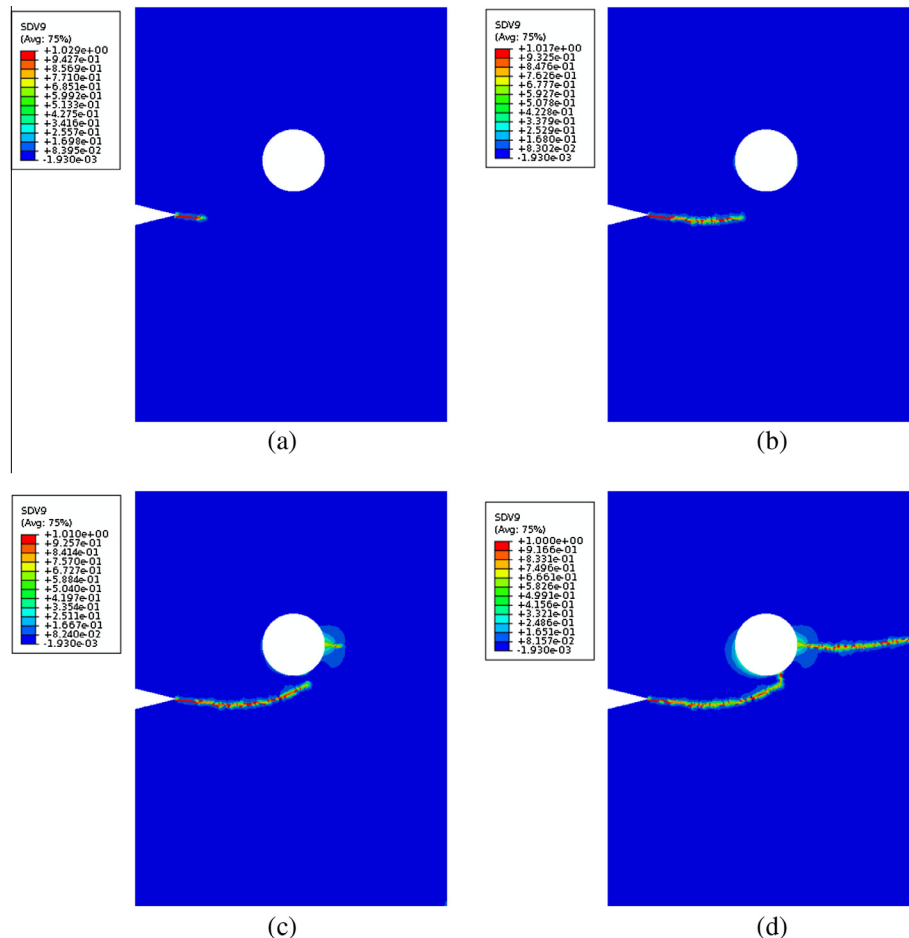


**Fig. 17.** Notched rectangular specimen with opening tension test. Crack propagation (a)–(d) for a mesh with 17,519 elements, element size $h$ = 3.0 mm with length-scale parameter $l$ = 6.5 mm.
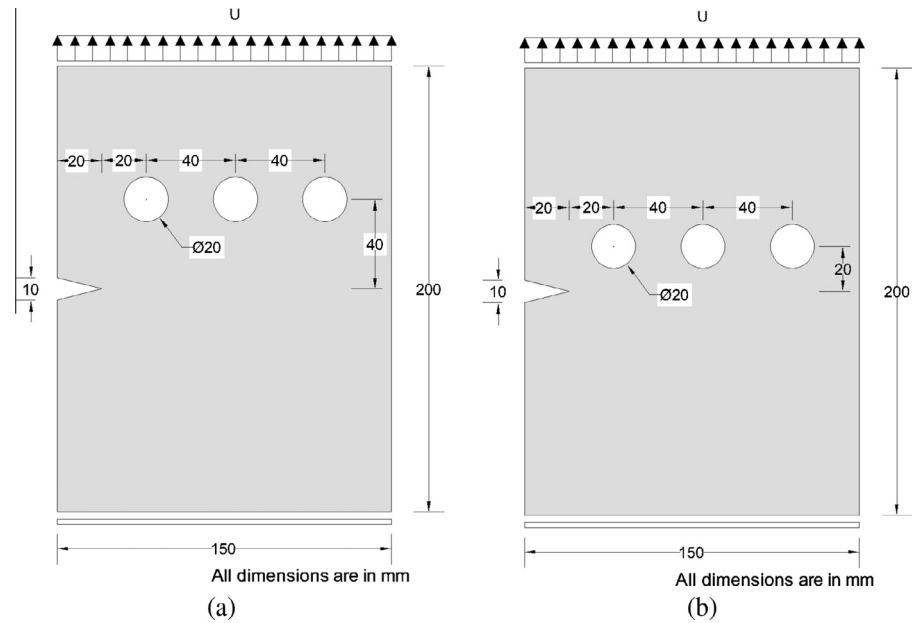
**Fig. 18.** Notched rectangular specimen with three openings. Geometry, loading and boundary conditions. (a) openings far from the initial notch and (b) openings near the initial notch.
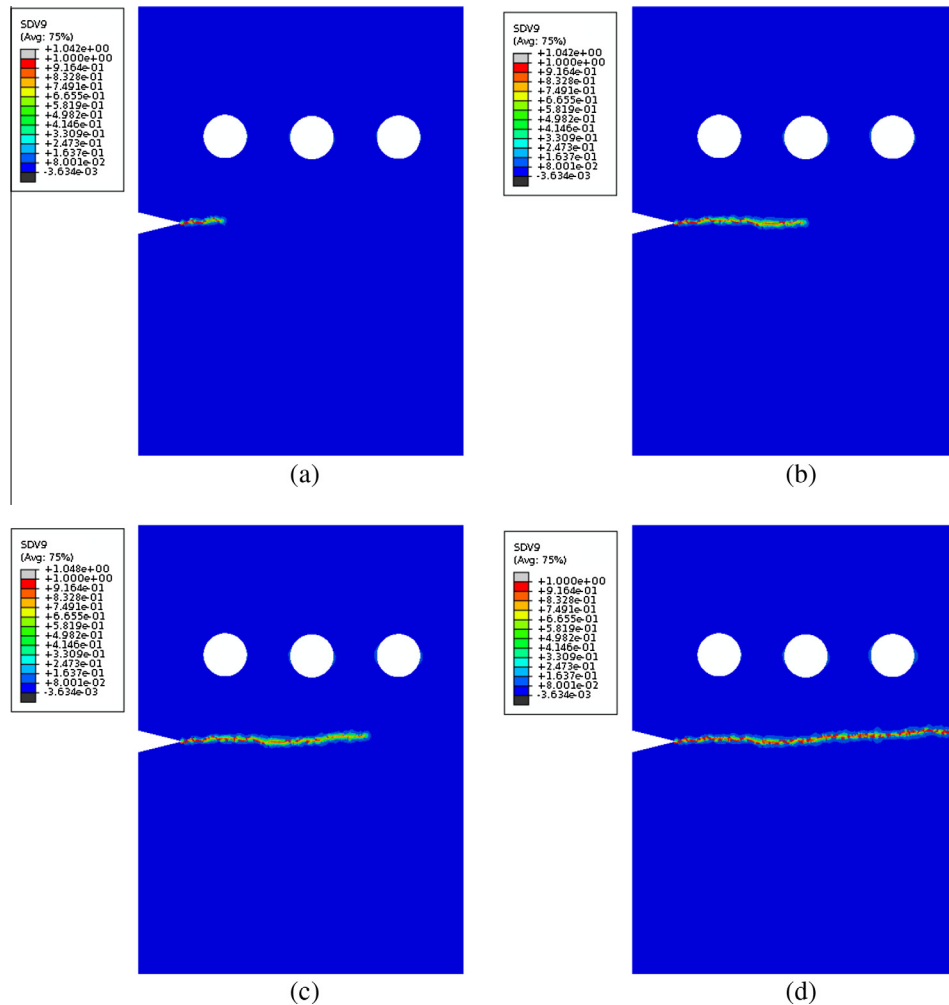


**Fig. 19.** Notched rectangular specimen with three openings tension sample in Fig. 18a. Crack propagation for a mesh with 18,926 elements, element size $h = 3mm$ with length-scale parameter $l = 8.5$ mm.
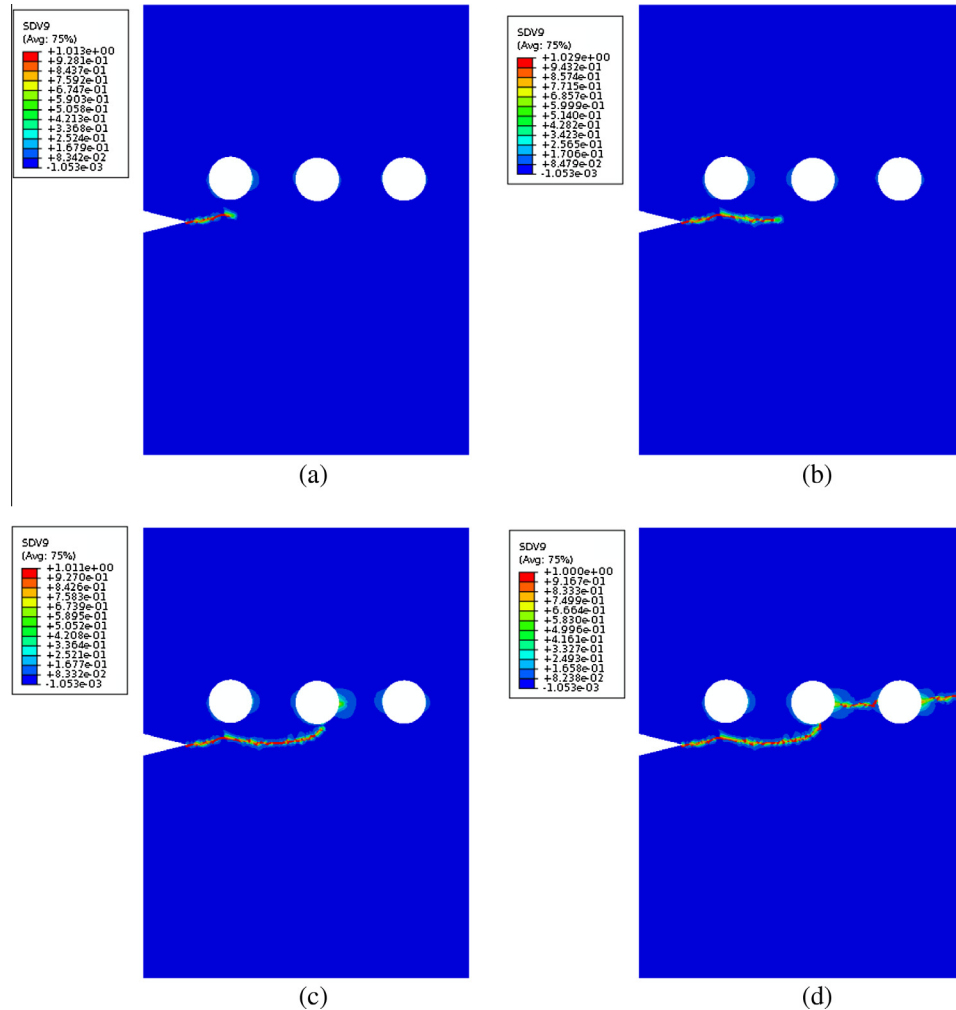
**Fig. 20.** Notched rectangular specimen with three openings tension sample in Fig. 18b. Crack propagation (a)–(d) for a mesh with 15,724 elements, element size h = 4 mm with length-scale parameter l = 8.5 mm.

### 5.4. Tension test of a notched rectangular specimen with one opening

In the following setup, we investigate the influence of the presence of openings to the resulting crack trajectory for a square plate subjected to tension. The numerical specimen consists of a notched rectangular plate with one opening, for which the geometry, boundary conditions and loading are given in Fig. 16. The setup is discretized using 17,519 quadrilateral elements of effective size $h = 3$ mm and material properties $E = 18$ GPa and $v = 0.2$. The length-scale parameter selected to be $\ell_0 = 6.5$ mm. Fig. 17 shows the crack propagation during the load increments. A state of stress is developed in the present setup, and in Fig. 17c the tip of the propagating has reached a location in the specimen that is nearly stress-free resulting in crack arrest. Propagation then resumes in the vertical direction as the failure load for the specimen is reached, as shown in Fig. 17d.

### 5.5. Tension test of a notched rectangular specimen with three openings

The next example demonstrates the effect of varying proximities of openings in altering the path of propagation of a crack. To do this we simulate two samples consisting of notched rectangular plates, each with three circular openings with centers aligned on a single horizontal line. In the first specimen, this line is situated

40 mm from the horizontal line emanating from the notch, while in the second specimen the distance has been reduced to 20 mm as shown in Fig. 18 along with the applied loading and boundary conditions. It can be seen in Fig. 19 that for holes situated significantly far away from the notch line the crack propagation is virtually unaffected by the presence of such features, whereas for sufficiently close openings the crack path is altered. We can also see from Fig. 20 that the presence of the opening nearest to the notch causes a kinking of the crack path just below it, however it is not near enough to the notch line as to arrest the crack propagation; this occurs just below the second opening along with the initiation of a new crack segment similar to what was observed in the previous example. The current example along with the preceding one shows a highlights another important strength of the phase-field method, specifically that the initiation of a crack does not require the introduction of a notch, and that a crack may initiate anywhere within the geometry of a given body.

## 6. Conclusion

In this paper we have presented a procedure for the implementation of the phase field model within the commercial FE code Abaqus for two-dimensional fracture problems. The implementation was based on the user element subroutine UEL and UMAT and enabled the modeling of different crack locations and orientations

using a mesh that is easily generated without the need to define initially bonded contact surfaces corresponding to a predefined crack path. The implementation of phase field model of fracture in Abaqus requires a new two dimensional element with three degrees of freedom per node, namely $u_x$, $u_y$ and $\phi$ with the first two corresponding to displacement degrees of freedom, while the third is for the phase-field. A UEL subroutine was used to implement this new element in the Abaqus library. An additional UMAT subroutine was also coded to enable the use of the Abaqus viewer to visualize results obtained from simulations utilizing the user-defined element. Several numerical examples were solved to demonstrate the merits of the implementation, in particular the ability of the phase-field method to realize non-trivial crack topologies with only minimal additional input to the mesh, such as refining the discretization at the vicinity of the expected crack in order to fulfill requirements regarding the ratio of element sizes to the chosen characteristic length of the phase-field.

## Acknowledgements

## References

[1] A. Griffith, Philos. Trans. Roy. Soc. Lond. A 221 (1921) 163–198.
[2] D. Ngo, A. Scordelis, J. Am. Concr. Inst. 64 (1967) 152–163.
[3] A. Ingraffea, V. Saouma, Fracture Mechanics of Concrete, Martinus Nijhoff Publishers, Dordrecht, 1985 (chapter Numerical modeling of discrete crack propagation in reinforced and plain concrete).
[4] J. Rice, J. Appl. Mech. 55 (1988) 98–103.
[5] X.P. Xu, A. Needleman, Int. J. Fract. 74 (1996) 289–324.
[6] F. Zhou, J. Molinari, Int. J. Numer. Methods Eng. 59 (2004) 1–24.
[7] N. Moës, J. Dolbow, T. Belytschko, Int. J. Numer. Methods Eng. 46 (1999) 131–150.
[8] N. Moës, A. Gravouil, T. Belytschko, Int. J. Numer. Methods Eng. 53 (2002) 2549–2568.
[9] L. Chen, T. Rabczuk, S. Bordas, G. Liu, K. Zeng, P. Kerfriden, Comput. Methods Appl. Mech. Eng. 209–212 (2012) 250–265.
[10] T. Rabczuk, S. Bordas, G. Zi, Comput. Struct. 88 (2010) 1391–1411.
[11] J. Rmmers, R. de Borst, A. Needleman, Comput. Mech. 31 (2003) 69–77.
[12] T. Rabczuk, T. Belytschko, Int. J. Numer. Methods Eng. 61 (2004) 2316–2343.
[13] T. Rabczuk, G. Zi, S. Bordas, H. Nguyen-Xuan, Comput. Methods Appl. Mech. Eng. 199 (2010) 2437–2455.
[14] Y. Rashid, Nucl. Eng. Des. 7 (1968) 334–344.
[15] R. Cope, P. Rao, L. Clark, P. Norris, Modelling of reinforced concrete behaviour for finite element analysis of bridge slabs, in: C. Taylor, E. Hinton, D. Owen (Eds.), Numerical Methods for Non-linear Problems I, Pineridge Press, 1980, pp. 457–470.
[16] L. Cedolin, Z.P. Bažant, Comput. Methods Appl. Mech. Eng. 24 (1980) 305–316.
[17] A. Hillerborg, M. Modéer, P. Petersson, Cem. Concr. Res. 6 (1976) 773–782.
[18] Z.P. Bažant, B.H. Oh, Mater. Struct. 16 (1983) 155–177.
[19] G. Francfort, J.J. Marigo, J. Mech. Phys. Solids 46 (8) (1998) 1319–1342.
[20] B. Bourdin, G. Francfort, J.J. Marigo, J. Mech. Phys. Solids 48 (2000) 797–826.
[21] B. Bourdin, G.A. Francfort, J.J. Marigo, J. Elasticity 91 (2008) 5–148.
[22] C. Kuhn, R. Müller, Eng. Fract. Mech. 77 (2010) 3625–3634.
[23] C. Kuhn, R. Müller, J. Theor. Appl. Mech. 49 (4) (2011) 1115–1133.
[24] G. Lancioni, G. Royer-Carfagni, J. Elasticity 95 (2009) 1–30.
[25] H. Amor, J.J. Marigo, C. Maurini, J. Mech. Phys. Solids 57 (2009) 1209–1229.
[26] C. Miehe, F. Welschinger, M. Hofacker, Int. J. Numer. Methods Eng. 83 (10) (2010) 1273–1311.
[27] C. Miehe, M. Hofacker, F. Welschinger, Comput. Methods Appl. Mech. Eng. 199 (2010) 2765–2778.
[28] R.J. Dorgan, A Nonlocal Model for Coupled Damage-Plasticity Incorporating Gradients of Internal State Variables at Multiscales Ph.D. Thesis, Department of Civil and Enviromental Engineering, Graduate Faculty of the Louisiana State University and Agricultural and Mechanical College, 2006.
[29] M.J. Borden, Isogeometric Analysis of Phase-field Models for Dynamic Brittle and Ductile Fracture Ph.D. Thesis, University of Texas at Austin, 2012.
[30] A.R. Ingraffea, M. Grigoriu, Probabilistic Fracture Mechanics: A Validation of Predictive Capability Tech. Rep. 90-8; Structural Engineering, School of Civil and Environmental Engineering, Cornell University Ithaca, New York; 1990.
[31] T. Bittencourt, P. Wawrzynek, A. Ingraffea, J. Sousa, Quasi-automatic simulation of crack propagation for 2D LEFM problems, Eng. Fract. Mech. 55 (2) (1996) 321–334.